



Contents lists available at ScienceDirect

Journal of Rock Mechanics and Geotechnical Engineering

journal homepage: www.jrmge.cn

Full Length Article

Impact of supercritical carbon dioxide on the frictional strength of and the transport through thin cracks in shale

Talal Al Shafloot^{a,*}, Arjun Kohli^b, Tae Wook Kim^b, Anthony R. Kavscek^b

^a College of Petroleum Engineering and Geosciences, King Fahd University of Petroleum and Minerals, Dhahran, Saudi Arabia

^b Energy Science & Engineering, Stanford University, Stanford, CA, USA

ARTICLE INFO

Article history:

Received 28 September 2023

Received in revised form

2 December 2023

Accepted 31 December 2023

Available online xxx

Keywords:

Supercritical carbon dioxide (sc-CO₂) carbon storage

Caprock

Fracture permeability

Friction coefficient

ABSTRACT

Understanding the mechanical and transport behavior of thin (i.e. small aperture) cracks slipping under supercritical carbon dioxide (sc-CO₂) conditions is essential to evaluate the integrity of sealing formations with buoyant sc-CO₂ below and the success of waterless fracturing. The two major items of interest in this work are frictional strength and permeability change of the crack. We used a triaxial cell that permits in situ visualization to conduct and monitor slippage along the faces of narrow cracks subjected to triaxial stresses. Such cracks are analogs to small geological faults. We tested carbonate-rich, 1-inch diameter Wolfcamp shale samples that are saw cut 30° to vertical to create a thin crack. Friction coefficients ranged from about 0.6 to 0.8 consistent with expectations for brittle rocks. The sc-CO₂ generally did not alter friction coefficient over the time scale of experiments. From a transport perspective, saturating cracks with sc-CO₂ substantially decreased permeability of the crack by 26%–52%, while slip resulted in a variety of permeability responses. Overall, the combined impact of sc-CO₂ saturation and slip reduced fault permeability for all tests. Our observations support the notion that the sealing capacity of some caprocks improves when saturated with sc-CO₂ and that some slip of small fractures is not necessarily detrimental to caprock integrity.

© 2024 Institute of Rock and Soil Mechanics, Chinese Academy of Sciences. Production and hosting by Elsevier B.V. This is an open access article under the CC BY-NC-ND license (<http://creativecommons.org/licenses/by-nc-nd/4.0/>).

1. Introduction

Shale formations are important for geological carbon dioxide (CO₂) storage because shales typically form the seal to prevent migration of buoyant fluids. It is critical during storage operations that vertical CO₂ permeation of the shale caprock seal, and accumulation underneath, does not trigger critically stressed faults and enhance the permeability of the seal. Likewise, it is important to understand if the transmissivity of fractures carrying CO₂ is different from other gases.

Additionally, shale formations are important for energy production. Due to low permeability, hydraulic fracturing of shales is needed to obtain economic recovery rates. Conventionally, water-based fluids are used to generate hydraulic fractures, but water has significant drawbacks including: permeability loss due to

capillary blockage or chemical reactions with shale minerals (Gundogar et al., 2021, 2022), and the environmental implications of injecting and disposing of millions of gallons water (Gandossi et al., 2013; Jew et al., 2017). Supercritical carbon dioxide (sc-CO₂) has been proposed as an alternative injectant for fracturing because it is low viscosity and nonaqueous (Middleton et al., 2015). For accurate predictions of storage and stimulation, it is essential to investigate fully fracture and fault behavior under sc-CO₂ conditions. From a waterless stimulation perspective, such understanding enables estimating the volumes to be injected and evaluating the stimulation efficiency.

1.1. Frictional strength of faults

Changing the pore pressure (P_p) within a geological formation changes the effective normal stress on faults and can result in fault slip (Streit and Hillis, 2004). Rock mechanical strength properties, such as the coefficient of sliding friction, are key inputs to estimate the risk of fault slip. Due to the difficulty of measuring these parameters in the field, many laboratory tests that simulate in situ conditions are conducted.

* Corresponding author.

E-mail address: shafloot@kfupm.edu.sa (T. Al Shafloot).

Peer review under responsibility of Institute of Rock and Soil Mechanics, Chinese Academy of Sciences.

<https://doi.org/10.1016/j.jrmge.2023.12.021>

1674-7755 © 2024 Institute of Rock and Soil Mechanics, Chinese Academy of Sciences. Production and hosting by Elsevier B.V. This is an open access article under the CC BY-NC-ND license (<http://creativecommons.org/licenses/by-nc-nd/4.0/>).

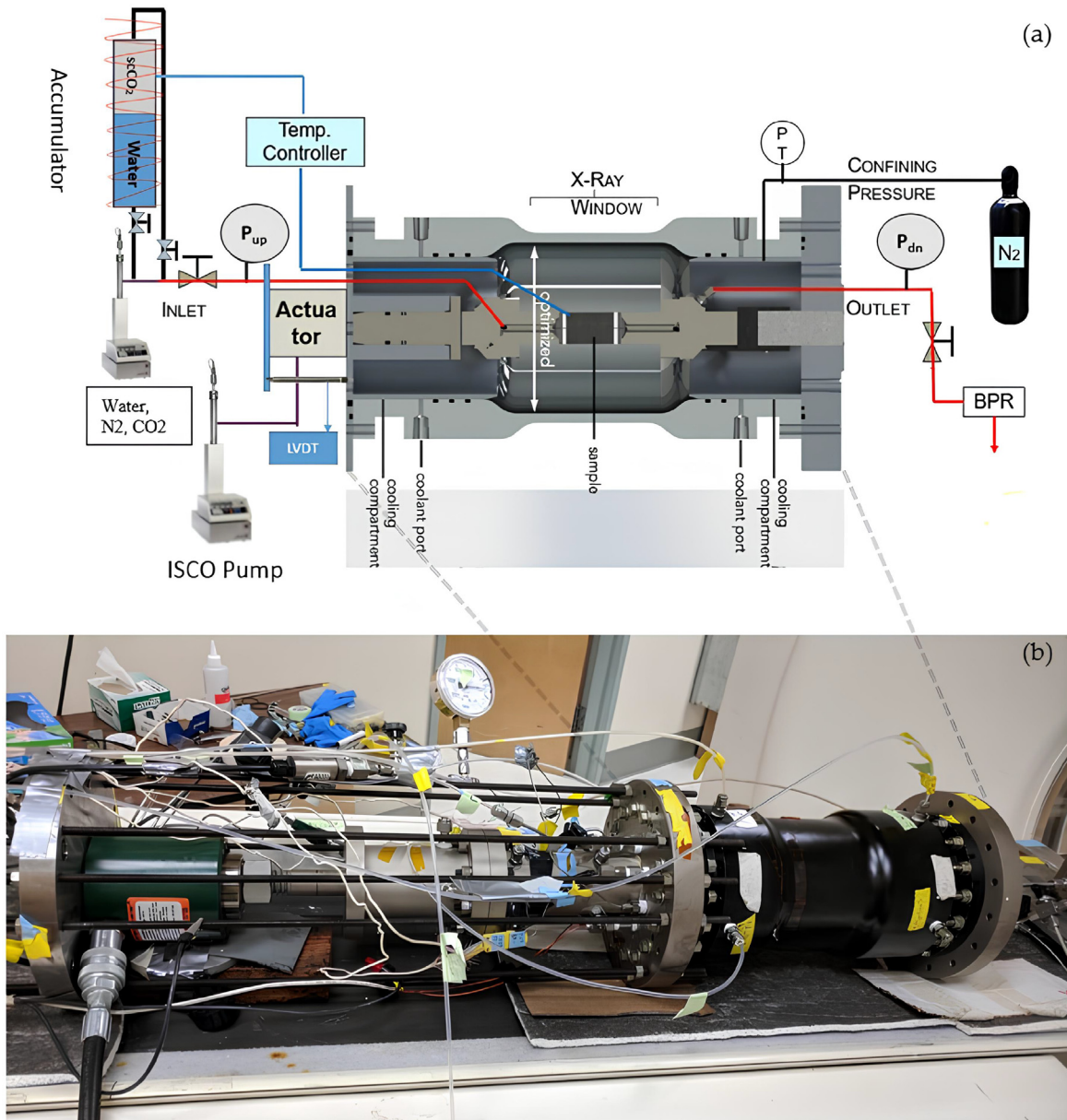


Fig. 1. Experimental setup: (a) Schematic of experimental triaxial cell (modified after Glatz et al. (2018)), and (b) Actual setup in the laboratory on the CT scanner positioning system.

Originally, Byerlee (1978) stated that the friction coefficient is independent of loading conditions and mineralogy with a range of 0.6–0.85. Nevertheless, studies concluded that mineralogy clearly influences frictional strength (Moore and Lockner, 2004; Crawford et al., 2008; Kohli and Zoback, 2013; Fang et al., 2018). Moreover, some studies highlighted the impact of the pore fluid on faults. For instance, Crawford et al. (2008) observed a difference in friction coefficient between wet (water saturated) and dry (argon saturated) samples; Spokas et al. (2019) reported lower friction coefficient measurements for samples saturated with reactive (acidic) brine. Hence, it is logical to expect an impact of $sc\text{-CO}_2$ on frictional strength, especially when components of shale rocks are reactive to CO_2 . For example, it has been reported that CO_2 exposure significantly reduces rock strength (Meng et al., 2021; Ozotta et al., 2022). A limited number of studies tested friction coefficient under $sc\text{-CO}_2$ conditions. Bakker et al. (2016) examined faults with sandstone and

carbonate rich gouges, Samuelson and Spiers (2012) tested gouges with various clay content, and Zhang et al. (2020) investigated fractures in sandstone samples. To our knowledge, few studies investigated CO_2 saturation and its impact on the frictional strength of shales.

1.2. Slip and fracture permeability

Permeability evolution during and after fault slip has been the interest of many studies. The permeability of a fault plane is governed by coupled factors such as mineralogy, effective stress, and surface characteristics. Permeability enhancement or reduction during slip depends on the characteristics of the fault surface. Interestingly, both permeability enhancement and reduction during slip is reported in the literature. Permeability increase was explained as an outcome of dilatation (Zhang et al., 2023a), mineral

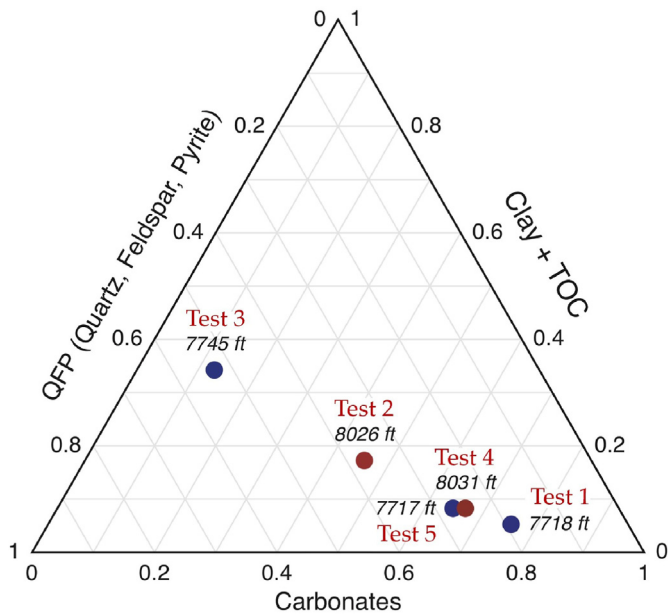


Fig. 2. Mineral composition of samples (wt%). Each point is tagged with the sample name, depth, and its test number.

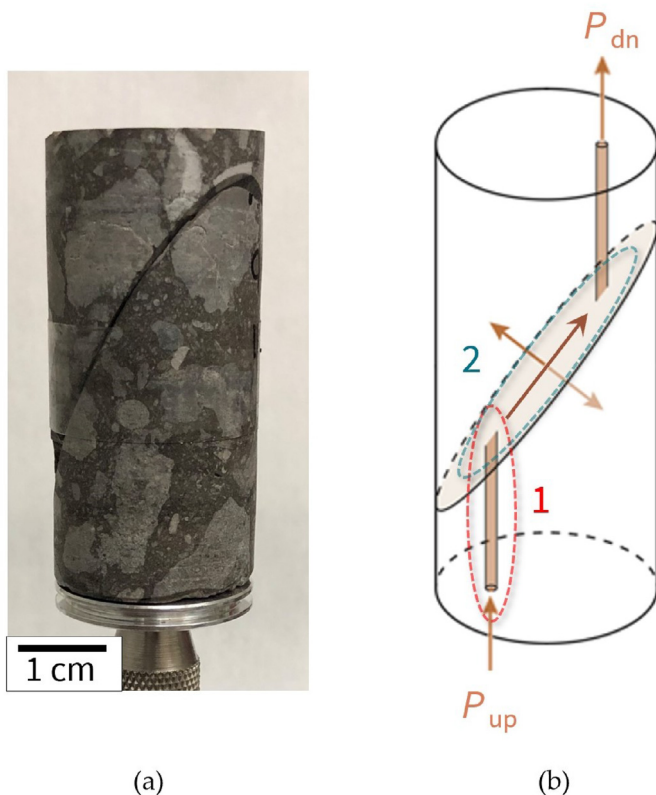


Fig. 3. Sample preparation: (a) An example of the final configuration, and (b) Schematic of sample configuration. The figure includes some demonstrations for Section 2.3.2.

dissolution (Polak et al., 2004; Foroutan et al., 2022), surface roughness evolution (Power et al., 1988), and self-propping of asperities (Bijay et al., 2023). Other studies assumed that the crack is sufficiently rough and potentially also at low effective normal stresses so that frictional wear debris are less likely to accumulate

(Yeo et al., 1998; Carey et al., 2015). On the other hand, permeability decrease is anticipated to result from asperity destruction and flow-restricting frictional wear development that overcomes dilatation (Taron and Elsworth, 2010; Rutter and Mecklenburgh, 2018; Spokas et al., 2019), precipitation of reaction products (Kolawole et al., 2021), and swelling of reactive clays (Jia et al., 2018).

In the case of sc-CO₂ saturation, fracture permeability and aperture were reported in the literature to be affected by adsorption induced swelling (Zhou et al., 2020), other CO₂-shale interaction induced mechanical alteration (Meng et al., 2021), and mineral dissolution (Gutierrez et al., 2015; Akono et al., 2019). During slip, permeability evolution has been reported in the literature to be impacted by the saturating fluid. For example, permeability evolution during slip demonstrated a difference when saturated with argon compared to brine (Crawford et al., 2008), and when saturated with an acidic brine (Spokas et al., 2019). The collective observations suggest exploring the combined effect of sc-CO₂ exposure and slip for faults. Nevertheless, a very limited number of studies investigated fault or fracture slip under CO₂ conditions.

1.3. Motivation

The literature review clearly indicates limited knowledge of the friction coefficient behavior under sc-CO₂ conditions for shale. Permeability evolution during slip requires further investigation to understand the contradicting observations in the literature. Moreover, the combined effect of slip and sc-CO₂ exposure of thin cracks in shale has not been investigated. To examine these points, we explored the frictional strength and permeability evolution of fractured shale slipping under dry CO₂ conditions. A saw-cut fracture is used as a model of a very small fault. We investigated the possible alteration of frictional strength caused by sc-CO₂ saturation. Furthermore, the combined effect of saturation and slippage on thin crack permeability was explored. Our high pressure high temperature cell allows us to examine behavior under moderate in situ conditions. Importantly, the high pressure high temperature cell combined with x-ray CT scanning allows visualization of diffusive gas transport.

2. Methodology

The methodology consists of a high pressure high temperature cell that is imaged using an x-ray CT scanner, and samples with well defined and reproducible fracture features. The procedure consists of saturating samples, inducing slip along the fracture, and measuring fracture transmissivity, as described next.

2.1. Experimental setup

Fig. 1a is a schematic of the experimental setup, while a photograph of the actual experimental setup is presented in Fig. 1b. The main high-pressure high-temperature cell is magnified (Fig. 1a) for clearer visualization of the interior components and sample configuration. The main cell was developed by Glatz et al. (2018), and it can accommodate temperatures up to 400 °C, a confining pressure of 13.8 MPa, and a 68.9 MPa axial stress. Upstream and downstream lines are connected to the sample for delivering and producing injected fluids. The downstream line is connected to a back pressure regulator to control pressure drop across the sample. Proper jacketing of core samples prevents communication between pore fluids and confining gas, N₂. We chose nitrogen due to its minimal X-ray attenuation and easier cleanup. Transducers (Model: PTX 1400) record upstream, downstream, and confining pressures with a ±0.15% accuracy.

An accumulator is used to pressurize and control sc-CO₂, with the aid of a Teledyne 500D ISCO pump. Axial stress is applied through the actuator, with the aid of another ISCO pump connected to a hydraulic piston. Actuator displacement is monitored using a Keyence GT2-P12K linear variable differential transducer (LVDT), that is installed on the upstream side, and it measures core vertical strain with 0.1 μm resolution. A temperature controller and thermal insulation is applied to the upstream line to maintain the upstream line at the desired temperature. Heat is applied to the sample using a mica heater. OMEGA thermo-couples (K type) record temperatures at the sample, upstream, cell wall, and accumulator.

2.2. Sample characterization and preparation

Samples tested are from the Wolfcamp shale in the Midland Basin, TX. Fig. 2 shows the mineralogical composition of the five samples by weight percent, where composition is measured with X-ray diffraction (XRD). Based on the classification of Sayers et al. (2019), three samples are silica-rich calcareous, one mixed siliceous, and one clay-rich siliceous shale. All samples have kerogen content less than 1% except for the clay-rich samples. From a petrophysical perspective, Rafatian and Capsan (2015) reported a low porosity range of 0–14 %, and wide range of matrix permeability with a maximum of less than 1 μD for similar samples. Finally, for our clay-content range, Young's modulus is expected to range between 40 GPa and 100 GPa (Zakhour et al., 2015).

Originally, samples were cored vertically with a one-inch diameter. After that, we introduced a saw-cut fracture angled 30° from vertical. We smoothed fracture faces using #100 alumina grit sandpaper. Next, the total sample length was adjusted to approximately 2 inches, and the two side faces were also smoothed with #100 alumina grit sandpaper (Fig. 3a). To ensure parallel-to-fracture flow, we drilled two 0.1-inch diameter bore holes in each half of the core. Bore holes are drilled in such a way that their intersection with the fracture allows for parallel to fracture flow for injected fluids. We highlight that the arrow parallel to the fracture represents flow inside the fracture, while arrows perpendicular to the fracture represents diffusion into the matrix (Fig. 3b). Before starting the wrapping (or jacketing) process, we dry the sample in a vacuum oven at a temperature of 45 °C for a minimum of two weeks. We chose this temperature to evaporate residual water in the sample while preserving clay minerals properties from alteration at very large temperatures.

Dry samples are attached to stainless steel endcaps and jacketed carefully prior to installation to prevent communication of pore fluid with confining fluid. Jacketing and sealing steps are summarized in Al Shafloot et al. (2021). Note that the final and most resistive layer during the wrapping process is a Viton sleeve. We chose a specific Viton sleeve that has minimal shear resistance to ensure no interference with stress measurements during slip. Viton 70 Durometer was purchased from Core Lab Instruments and it has the dimensions of 1 inch diameter and 0.1875 inch wall thickness.

2.3. Experimental procedure

We designed our experimental procedures to serve several purposes. Some aspects are presented in this work, while the rest are available in Al Shafloot (2022). For instance, steps that aim to investigate temporal saturation change with the aid of CT scanning along with their analysis and interpretation is part of another undergoing study. The major steps applied are as follows.

1. Scan the sample using x-ray micro-CT at a resolution of about 28 μm. This step is performed prior to installation within the main cell, and post experiment. The goal is to observe structural

changes in the sample. A Zeiss Xradia 520 Versa X-ray micro-CT was used with source parameters of 140 kV voltage and 0.071 mA current. An optimum field of view of 28 mm resulted in a 28 μm × 28 μm × 28 μm voxel resolution.

2. Saturate the sample with krypton (Kr). Saturating with Kr helps quantify gas-accessible porosity and visualize diffusion processes due to the large CT number of Kr. CT scanning was conducted using a GE HiSpeed CT scanner. The scanner was operated using a 120 mA tube current and 140 kV voltage. The field of view captured is 10 cm with 195 μm × 195 μm × 625 μm voxel resolution.
3. Saturate the sample with CO₂. Injecting CO₂ helps to visualize the displacement of Kr by CO₂, and helps to quantify CO₂ storage capacity.
4. Induce slip. Monitoring stresses and flow rate of injected CO₂ helps to quantify the friction coefficient and monitor permeability evolution.
5. Measure permeability. Measurement at specific stages investigates the permeability change as a consequence of targeted factors.
6. Measure fracture surface roughness. This step is conducted to the samples after disassembling the setup. Calculating surface roughness aids investigation of its correlation to frictional strength and permeability evolution behaviors.

After installing the sample in the main cell, the following sequence of experimental steps is typically performed. We start the experiment by applying vertical and confining stresses and set values to a state that serves the purpose of the test. For incremental controlled axial displacement tests, stress configurations are set to prevent fault slip at the maximum pore pressure to be applied (1300 psi). Thereafter, the sample is vacuumed long enough to ensure extraction of residual fluids. Following that, we saturate the sample with Kr for 4–5 d. Next, we saturate the sample with CO₂ for 4 d. During this period, we measure initial, intermediate and final fracture permeabilities prior to slip. Then, we induce slip on the fracture and measure permeability at holding periods separating slip intervals. We continue saturation with CO₂ for another three days and monitor fault permeability. Finally, we vacuum evacuate the sample for at least 48 h. Throughout, we continuously use CT scanning to visualize slip on the fracture.

We emphasize that samples are dry to meet study objectives to investigate CO₂-rock interactions in the absence of reactivity. In situ shale conditions are partially or fully saturated with brine. CO₂-saturated brine is acidic and expected to be reactive. Our objective is to isolate the expected strong reactivity in the presence of brine, and investigate only the CO₂-rock interaction. Our results, to follow, help us to understand the behavior when CO₂ is injected into dry gas shale formations and, importantly, our work is useful for benchmarking to investigate the impact of reaction when brine-saturated samples are tested in the future.

2.3.1. Inducing slip

For our sample configuration, the resolved shear stress (τ), normal stress (σ_n), and friction coefficient (μ) are calculated using the following equations (Tembe et al., 2010):

$$\left. \begin{aligned} \tau &= \frac{1}{2}(\sigma_1 - \sigma_3)\sin 2\theta \\ \sigma_n &= \frac{1}{2}[(\sigma_1 + \sigma_3) - (\sigma_1 - \sigma_3)\cos 2\theta] - P_p \\ \mu &= \frac{\tau}{\sigma_n} \end{aligned} \right\} \quad (1)$$

Table 1
Summary of the experimental conditions for measuring permeability.

Parameter	Value	Unit
Temperature	45	°C
Confining pressure	1800	psi
Average pore pressure	1300	psi
Steady-state $P_{up} - P_{dn}$	5–50	psi
Modified pulse decay $P_{up} - P_{dn}$	50–100	psi

where σ_1 is the axial stress, σ_3 is the horizontal stress, P_p is the pore pressure, and θ is the fault angle to vertical. In our system, σ_3 is equal to the confining stress.

The target of our study was to induce slip by an incrementally controlled axial displacement with an increment of 0.5 mm. We needed, however, to determine the maximum total vertical displacement that does not cause failure to the core jacket. Hence, we decided to induce the slip for Test #1 by applying a large pore pressure to a critically stressed fault. Before injecting CO₂ at 1300 psi (8.96 MPa), we applied 24 MPa axial stress and a confining stress of 1800 psi (12.41 MPa). When a pressure of 1300 psi was applied on the upstream side, the fracture slipped a total axial distance of 2.7 mm. Jacketing did not fail by the end of the slip, that is an indication of a safe total vertical displacement for constant axial displacement tests.

Based on our findings in Test #1, we designed the controlled axial displacement rate tests to induce a total parallel to fracture displacement of 2.5 mm, with five equal increments of 0.5 mm. For each displacement increment, we applied a constant vertical displacement rate of 1.0 $\mu\text{m/s}$ (around 1.2 $\mu\text{m/s}$ parallel to fault). Following each increment, a hold period was implemented to measure permeability. The initial conditions of slip increments are 14.4 MPa axial stress (σ_1), 12.4 MPa confining stress (σ_3), 3.9 MPa normal stress (σ_n). It is worth mentioning that slippage is conducted on fractures saturated with sc-CO₂ for four days.

Our experimental setup and sample configuration require important corrections for accurate measurements (Tembe et al., 2010). The two major corrections to measured stresses are corrections related to true area of contact and jacket strength. For the former, we applied this correction to calculated shear and normal stresses by considering axial shortening (Scott et al., 1994). In fact, this correction is insensitive to μ and σ_n because both are divided by the same correction factor. Regarding the latter, Tembe et al. (2010) estimated that an addition of 0.013 to the calculated friction coefficient is needed as a consequence of the polyurethane jacketing resistance by the end of 9.2 mm fault slip. Subsequently, because the jacketing material (Viton) has, at most, a stiffness similar to polyurethane, and we slip our samples to a total of around 2.2 mm parallel to slip distance, we expect a negligible interference with the friction coefficient calculations that are within the uncertainty error. Finally, the complexity of our system does not allow a dynamic adjustment of confining pressure to preserve a unified and

Table 2
Summary of steps accomplished in each test.

Test number	Slip approach	Transmissivity evolution	
		Saturation effect	Slip effect
1	pore pressure induced	✓	
2	Controlled axial displacement	✓	✓
3	Controlled axial displacement	✓	
4	Controlled axial displacement	✓	✓
5	Controlled axial displacement	✓	✓

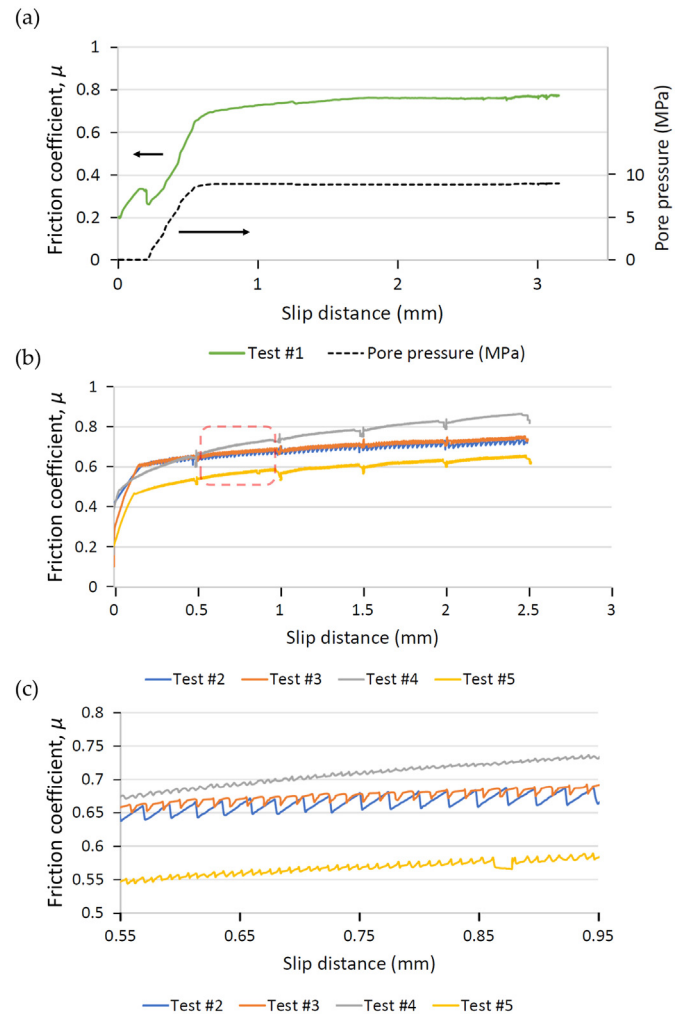


Fig. 4. Friction coefficient profiles: (a) hydraulically induced slip, (b) controlled axial displacement induced slip, and (c) illustration for a variety of stick-slip behavior for tests in (b).

constant normal stress. This resulted in measuring friction coefficient at a normal stress range of 5.92–7.59 MPa. This is a small and reasonable difference of σ_n for the measured friction coefficient (μ). Furthermore, Ikari et al. (2009) reported consistent friction coefficient values for faults slipping over a wide normal stress range of up to 60 MPa.

Table 3
Summary of frictional strength parameters.

Test #	Clay + TOC (w %)	Initial Friction Coefficient		Maximum Friction Coefficient		Δ Friction coefficient (maximum-initial)
		Magnitude	Normal stress σ_n (MPa)	Magnitude	Normal stress σ_n (MPa)	
1	5.4	0.64	6.2	0.77	6.58	0.13
2	16.87	0.6	5.6	0.73	6.41	0.13
3	33.76	0.6	5.5	0.75	6.38	0.15
4	7.77	0.48	5.14	0.86	7.59	0.38
5	7.92	0.47	5.08	0.64	5.92	0.17

2.3.2. Measuring transmissivity

Several studies in the literature calculated fracture permeability utilizing the cubic law (Witherspoon et al., 1980; Zimmerman and Bodvarsson, 1996; Germanovich and Astakhov, 2004). Rather than the steady-state approach, some studies applied the pulse decay (Wu et al., 2017) and pressure oscillation methods (Rutter and Mecklenburgh, 2018). Nevertheless, calculating fracture permeability for all methods requires the knowledge of very sensitive parameters that are hard to quantify accurately such as fracture tortuosity and the variation in effective aperture. Furthermore, in our fault configuration, the upstream pump drives the injected fluids to flow from a source (upstream wellbore) to a sink (downstream wellbore) through elliptical fracture faces.

Rutter and Mecklenburgh (2018) derived equations to calculate fracture transmissivity for a fracture configuration similar to our study, with steady-state, pressure oscillation, and pulse decay approaches. Their derivation is based on the analogy that the flow of a viscous fluid through a conductive crack is analogous to the electric current flow through a resistive layer enclosed by an insulating medium. Transmissivity has dimensions of L^3 , and it can be seen as the product (kt) of fault permeability k_f (m^2) multiplied by its thickness w (m).

It is worth clarifying some confusing aspects in the approach of Rutter and Mecklenburgh (2018). The transmissivity term they derived is different from the one discussed in hydrology or reservoir engineering. While Rutter and Mecklenburgh (2018) utilizes transmissivity as fluid transport capacity, there are various definitions of transmissivity in hydrology. The closest definition to the Rutter and Mecklenburgh (2018) approach in hydrology is the product of the thickness of aquifer and the average value of hydraulic conductivity (K) (Freeze and Cherry, 1979). Nevertheless, the dimension of transmissivity is L^2/T in hydrology against L^3 in Rutter and Mecklenburgh (2018). Another confusing point is the notation of transmissivity. The introduced parameter (kt) denotes

thickness to t , while the convention is denoting time to t . To avoid the confusion, we substituted the parameter kt with kh .

To determine the proper permeability measuring approach, we conducted pretests to measure permeability of shale samples with vertical natural fractures. Findings from those pretests suggest that applying the steady-state approach is sufficient. For the steady-state case, Rutter and Mecklenburgh (2018) derived the following equation:

$$\left. \begin{aligned} Q &= \frac{\Delta P kh}{\eta} \frac{B\pi}{\log_e\left(\frac{2a}{r_0} - 1\right)} \\ B &= \frac{2}{\pi} \tan^{-1}(2n) \end{aligned} \right\} \quad (2)$$

where kh is transmissivity (dimension of L^3), Q is the flow rate, ΔP is the pressure difference across the samples, η is the viscosity, r_0 is the wellbore radius, and a is half the distance between wellbores. Interpretation of the parameter n and a full derivation of the equation is provided by Rutter and Mecklenburgh (2018).

While the steady-state approach is our default approach, the pulse decay method is utilized when very small flow rates are observed with steady-state. Fault transmissivity can be calculated using the equation derived by Rutter and Mecklenburgh (2018) for pulse decay tests as

$$\left. \begin{aligned} kh &= \frac{\eta \beta_D}{\pi} M \frac{\log_e\left(\frac{2a}{r_0} - 1\right)}{B} \\ \beta_D &= V_D \kappa_f \end{aligned} \right\} \quad (3)$$

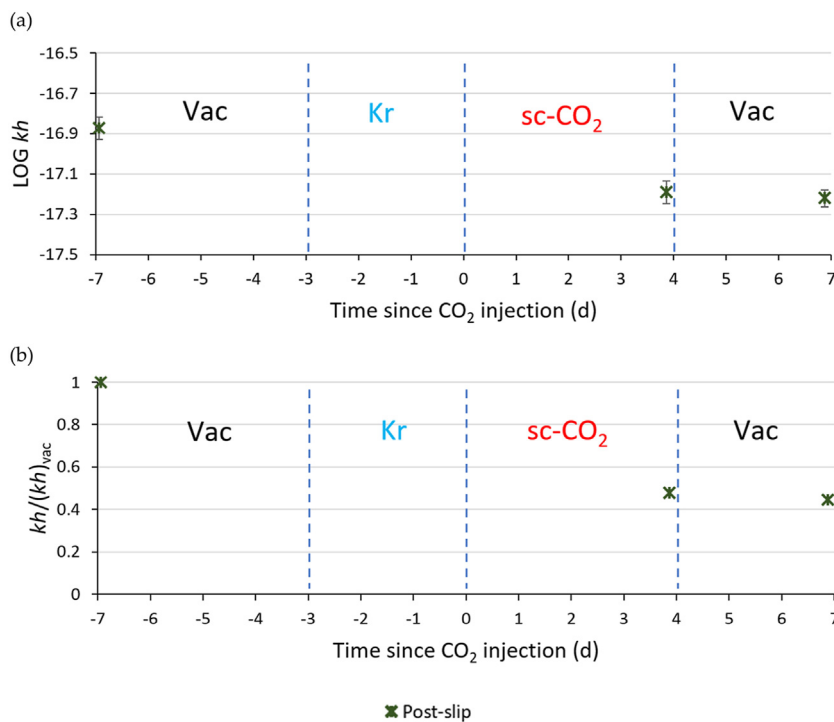


Fig. 5. Transmissivity measurements for Test #1 (a) log of transmissivity, and (b) change of transmissivity relative to first measurement.

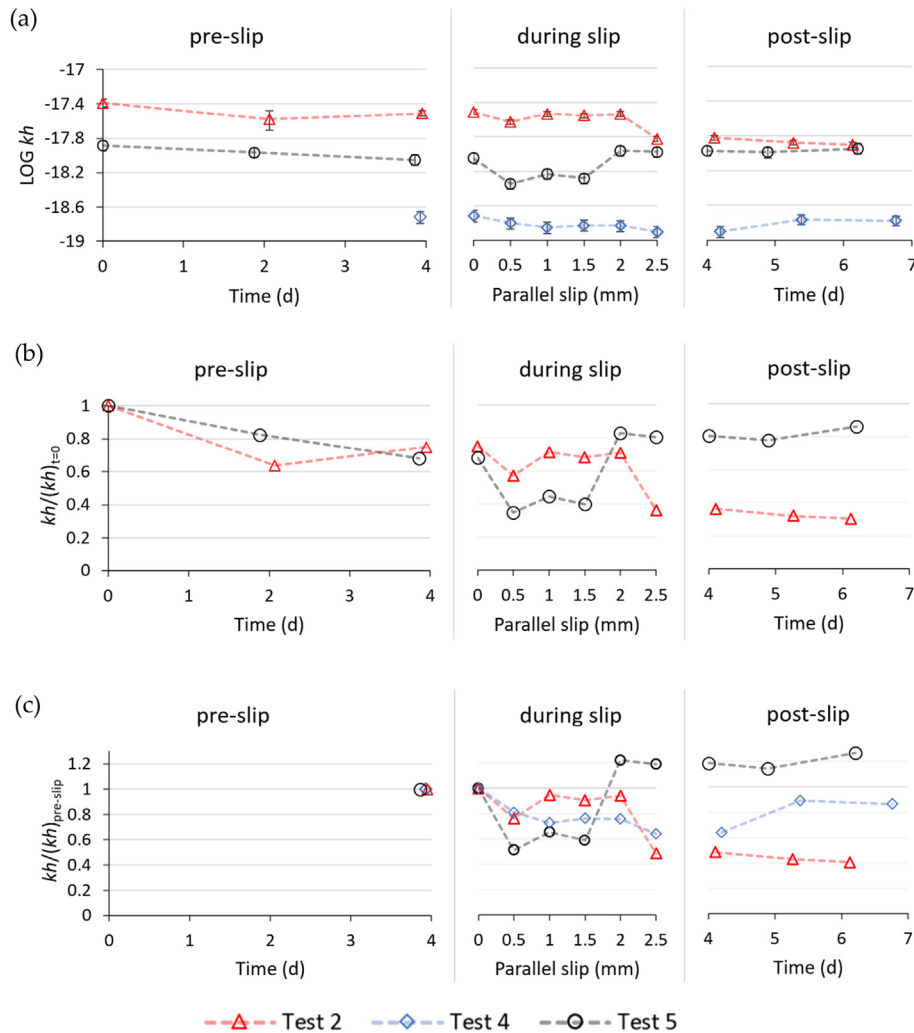


Fig. 6. Transmissivity measurements for Tests #2, 4 and 5 (a) log of transmissivity, (b) relative change of transmissivity to first measurement, and (c) change of transmissivity relative to pre-slip measurement. Injection of CO₂ happens at $t = 0$.

where β_D is the downstream storativity, V_D is the downstream volume, and κ_f is the fluid compressibility. M can be obtained from the transport equation solution:

$$\frac{P(t)}{P(0)} = \exp(-f_1 Mt) \quad (4)$$

where $P(t)$ is the time-dependent pressure amplitude, $P(0)$ is the pressure amplitude at time equals zero, f_1 is a function that accounts for non-zero sample porosity, and t here is time. Because sample porosity is negligible compared to large downstream volume, f_1 is set to 1. Hence, M is the slope of the straight line in $\log_e(P(t)/P(0))$ versus time plot.

We measured the transmissivity at a constant confining stress of 12.4 MPa, 1300 psi (8.96 MPa) pore pressure, and 45 °C temperature. In the steady-state case, for each permeability measurement, we applied three different ΔP magnitudes ($\Delta P = P_{up} - P_{dn}$) that range between 15 and 50 psi (0.103–0.345 MPa) to test the applicability of the steady-state method, that can be reflected by a linear relationship between pressure differential and flow rate. Moreover, laminar flow was validated for all samples by calculating the Reynolds number (Re) at two zones within the sample including the

flow inside the 'borehole' (zone 1) and along the fault (zone 2 in Fig. 3b). Because of time constraints during slip, however, we only apply the largest ΔP prior to slip at holding periods between slip increments. When the pulse decay method is implemented, a single ΔP that ranges between 50 and 100 psi (0.345–0.689 MPa) is applied at each measurement. Upstream and downstream pressures are set in such a way that their average is equal to 1300 psi (8.96 MPa). Table 1 summarizes the experimental conditions for measuring permeability.

3. Results

Table 2 summarizes the steps accomplished in each test. Test #1 is considered as a pilot test to help planning the following tests.

3.1. Frictional strength

Fracture slippage was induced hydraulically for Test #1 as described above (Section 2.3.1). Fig. 4a depicts the friction coefficient profile during slip. The moment pore pressure was increased, the fracture started slipping at an average rate of 15 $\mu\text{m/s}$ until a total slip distance of 1.5 mm. After that, the slip rate started

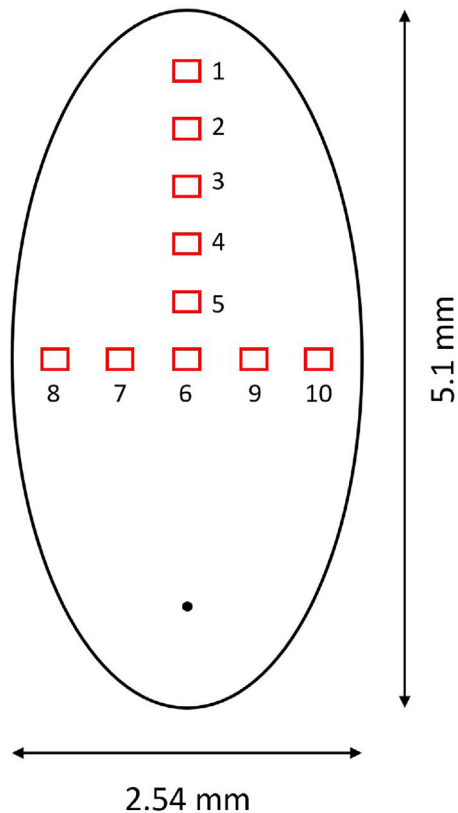


Fig. 7. An illustration of fracture zones scanned for roughness measurements within the fault.

decreasing gradually to reach a variable low rate with an average of approximately $0.4 \mu\text{m/s}$. When the friction coefficient profile demonstrated a plateau for a considerable slip distance, we stopped the ISCO pump controlling axial displacement to protect the jacket integrity. A total slip distance of 3.15 mm was achieved.

An incremental constant slip rate was successfully applied in Tests #2 to #5. Fig. 4b illustrates the friction coefficient profiles. As expected, all profiles start with a sharp increase indicating elastic loading of the fault, followed by a sharp decrease in the slope corresponding to the initiation of fracture slip. Friction coefficient curves demonstrate a continuously small increase until the end of tests, that is an outcome of strain hardening. During holding periods, a small amount of stress relaxation is observed. Zooming into friction coefficient profiles, we see a tooth-like pattern that indicates a chaotic stick-slip response (Fig. 4c). The observed chaotic bounded oscillation is an indication of a transition stage from stable to cyclic stick-slip loading. Such behavior is observed in the literature for smooth fractures (Zhang et al., 2023b; Meng et al., 2023), and it is dependent on the micro-roughness of the surface, normal stress, and the displacement-controlled loading rate (Zhang et al., 2023b). This chaotic stick-slip behavior varies between tests since it is extremely sensitive to the material properties and stiffness. Importantly, our tests indicate that chaotic stick-slip loading happens under our range of initial normal stress (5–6.2 MPa) and loading rate ($1.0 \mu\text{m/s}$). Such an observation can be useful to the undergoing research of the loading behavior prediction under various conditions.

Table 3 summarizes the frictional strength parameters. Each sample exhibits a different behavior in at least one of the aspects: initial friction coefficient (by end of elastic loading zone), friction coefficient change during slip (hardening rate), maximum friction coefficient, and the amplitude of chaotic stick-slip behavior (Fig. 4). We examined possible correlations of these parameters to mineralogy.

3.2. Fracture transmissivity

We measured the transmissivity at different stages of the experiments trying to investigate the impact of three factors: saturating with sc- CO_2 , fault slippage, and holding after slippage. We measured transmissivity with the steady-state approach for Tests # 1, 2 and 5. For Test #4, we implemented the modified pulse decay approach. Unfortunately, minor failure of jacketing resulted in a small leakage rate of confining fluid (N_2) into the sample, that does not allow calculating the transmissivity for Test #3.

Because Test #1 was conducted to determine the maximum axial displacement by inducing slip hydraulically, we measured permeability after slippage with the focus on the effect of saturation on permeability. Fig. 5 depicts transmissivity measurements during the test. We measured permeability right after slip with nitrogen (N_2). By the end of the CO_2 saturation period, we measured kh with CO_2 . Finally, we checked kh after three days of vacuuming. Overall, these transmissivity measurements are considered large compared to measurements in Rutter and Mecklenburgh (2018), especially for fractures undergoing slippage (Fig. 5a). The transmissivity at the end of sc- CO_2 saturation demonstrated a significant drop of 52% as a combined influence of K_r and sc- CO_2 (Fig. 5b). In fact, it is logical to consider this impact to be mostly a result of sc- CO_2 , because it has larger adsorption capacity than K_r (Aljamaan et al., 2017). Finally, the kh value obtained by injecting N_2 revealed a magnitude similar to the previous point thereby indicating a permanent permeability reduction.

Transmissivity measurements of controlled axial displacement tests are shown in Fig. 6. It is seen that kh magnitudes of Test #4 is approximately one order of magnitude smaller than Tests #2 and 5,

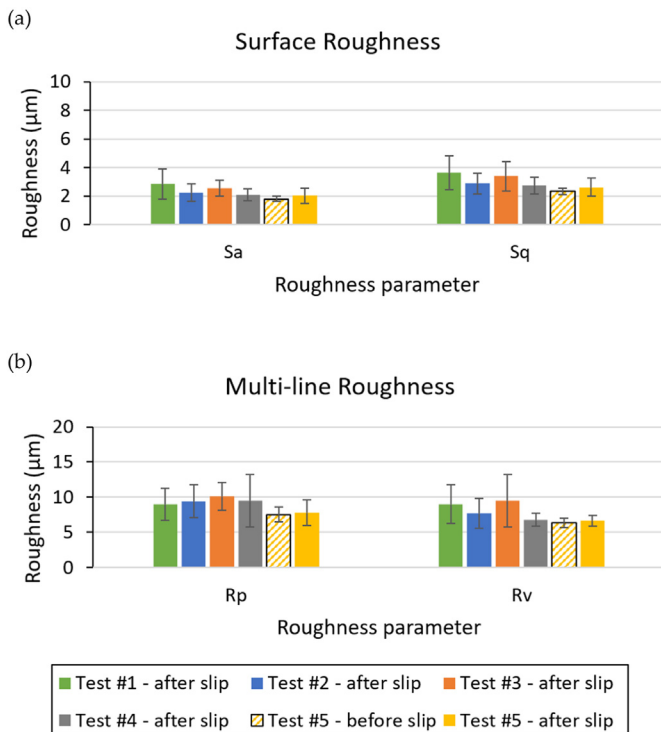


Fig. 8. Roughness measurements (a) Surface parameters S_a and S_q , and (b) Multi-line parameters R_p and R_v .

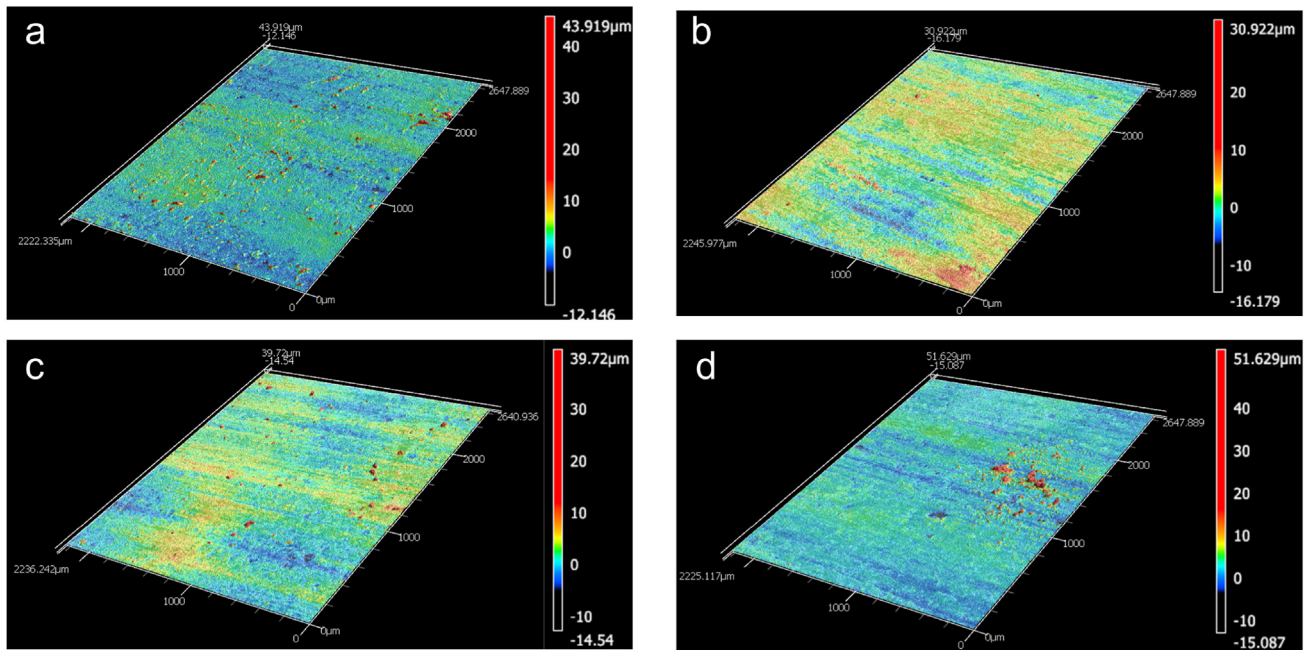


Fig. 9. Illustration of debris formation through surface mapping for (a) Test #2, (b) Test #3, (c) Test #4, and (d) Test #5. Warmer colors indicate greater asperity height.

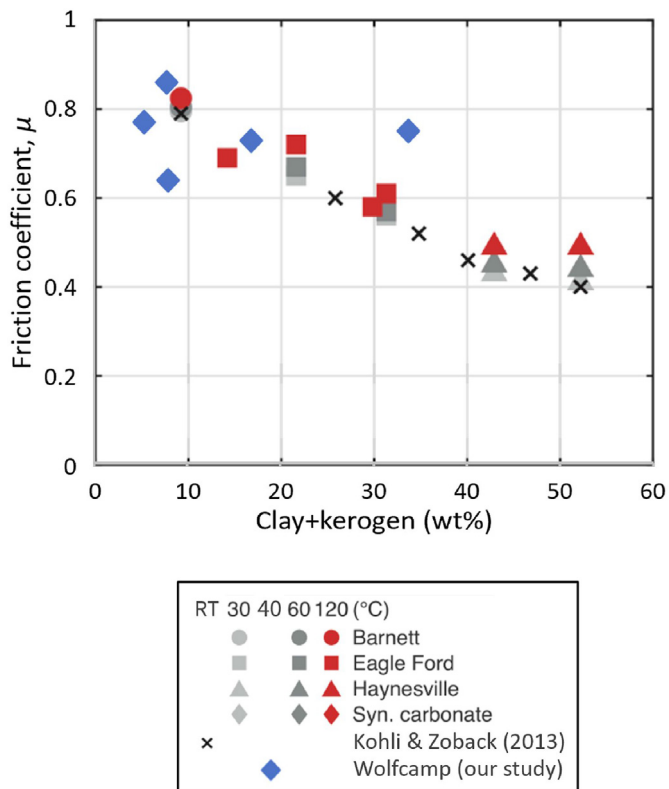


Fig. 10. Comparison of our friction coefficient values to (Zoback and Kohli, 2019).

supporting our decision for utilizing a modified pulse decay for this test. Overall, samples demonstrated permeability reduction after short-term relaxation of slipped faults under sc-CO₂ conditions (Fig. 6a). Fig. 6b presents the relative change of kh to the value at the beginning of sc-CO₂ saturation. Saturation for four days is

responsible for a transmissivity decrease of 26% and 32% for Tests #2 and 5, respectively.

To study the impact of fault slip and relaxation afterward, we plotted the kh change relative to values pre-slip (Fig. 6c). At the first slip increment, transmissivity decreases for all tests. For intermediate increments, there is a recovery trend in kh measurements. By the end of 2.5 mm slip, two samples (Tests # 2 and 4) demonstrated a permeability reduction, while Test #5 showed a permeability enhancement. Holding after slippage resulted in both responses of transmissivity recovery (Test #4 and 5) and further reduction (Test #2). We hypothesize that larger clay-content of the sample in Test #2 caused a creep and stress relaxation that narrows flow paths within the fault.

3.3. Surface roughness

We measured surface roughness using a Keyence VK-X Series 3D laser scanning confocal microscope. This instrument provides an xy resolution of 0.5 nm, and a lateral (z -direction) resolution of 120 nm. To provide a representative measurements, we scanned 10 areas with x and y dimensions of 1.4 mm and 1.2 mm, respectively. Fig. 7 provides the configuration of scanned zones on the fault surface.

For each sample, we measured several parameters using both multi-line and surface roughness approaches. Parameters measured are arithmetic average (S_a), quadratic average (S_q), maximum peak height above the mean line (R_p), and maximum valley depth below the mean line (R_v). We chose the approach (multi-line (R) or surface (S)) based on what we believe is more suitable to describe the fracture surface characteristics. An arithmetic average is the most widely used parameter and it is not influenced by outliers and noise. On the other hand, a quadratic average gives greater weight to larger measurements. Finally, averaged peak and valley measurements reveal insights about potential asperities.

Roughness parameters are calculated using the following equations as

$$S_a = \frac{1}{A} \iint_A |z(x,y)| dx dy \quad (5)$$

$$S_q = \sqrt{\frac{1}{A} \iint_A z^2(x,y) dx dy} \quad (6)$$

$$\left. \begin{aligned} R_{p_i} &= \max z(x) \\ R_p &= \frac{\sum_{i=1}^n R_{p_i}}{N} \end{aligned} \right\} \quad (7)$$

$$\left. \begin{aligned} R_{v_i} &= \min z(x) \\ R_v &= \frac{\sum_{i=1}^n R_{v_i}}{N} \end{aligned} \right\} \quad (8)$$

where A is scanned area and N is the number of assessed lines. Each multi-line roughness measurement is assessed over 31 equally spaced lines to cover the entire sample.

We measured roughness for all samples after conducting the experiment. The sample in Test #5 is the only sample with roughness measured prior to the test. Fig. 8 summarizes roughness parameters. Arithmetic (S_a) and quadratic averages of post-test samples (S_q) demonstrated minor differences in roughness, with averages around 2.4 μm and 3 μm for S_a and S_q , respectively as shown in Fig. 8a. In addition, maximum peak height (R_p) and valley depth (R_v) in like manner revealed similar measurements, with averages that range between 6 and 10 μm (Fig. 8b). It is likely that surfacing with grit #100 resulted in very smooth surfaces that are difficult to deform during slip. In fact, comparing prior and post-slip roughness parameters for Test #5 showed minimal change to the averages, but considerable increase to the standard deviation of 10 measurements. This might be an outcome of the debris generated during slip, that is observed in height measurements by local abnormal peaks (Fig. 9).

4. Discussion

4.1. $sc\text{-CO}_2$ influence on frictional strength

Friction coefficient (μ) is the main parameter of interest in the literature because it determines the required ratio of stresses to initiate a slip event. This study presents friction coefficient magnitudes for variety of carbonate-rich, mature samples, with a variety of clay-content that approximates actual field percentages. Overall, our measurements fall within the upper side of the values reported in the literature.

Fig. 10 compares the friction coefficient values in this study to results in the literature (Zoback and Kohli, 2019). Data of Zoback and Kohli (2019) are collected for organic-rich shales from Texas reservoirs (Kohli and Zoback, 2013) and they performed slip up to 5 mm. They conducted slip tests utilizing sandstone forcing blocks filled with dry shale gouges with various clay + kerogen content under no pore fluid pressure. Our data shows a good match to the two studies for low clay + kerogen content. However, this is not the case for the high clay + kerogen content sample. Furthermore, our data does not demonstrate a similar behavior of decreasing friction coefficient as clay + kerogen content increases. In fact, our friction coefficient magnitudes are almost independent of clay content.

Correlations of friction coefficient versus clay content have been reported in the literature (Crawford et al., 2008; Tembe et al., 2010;

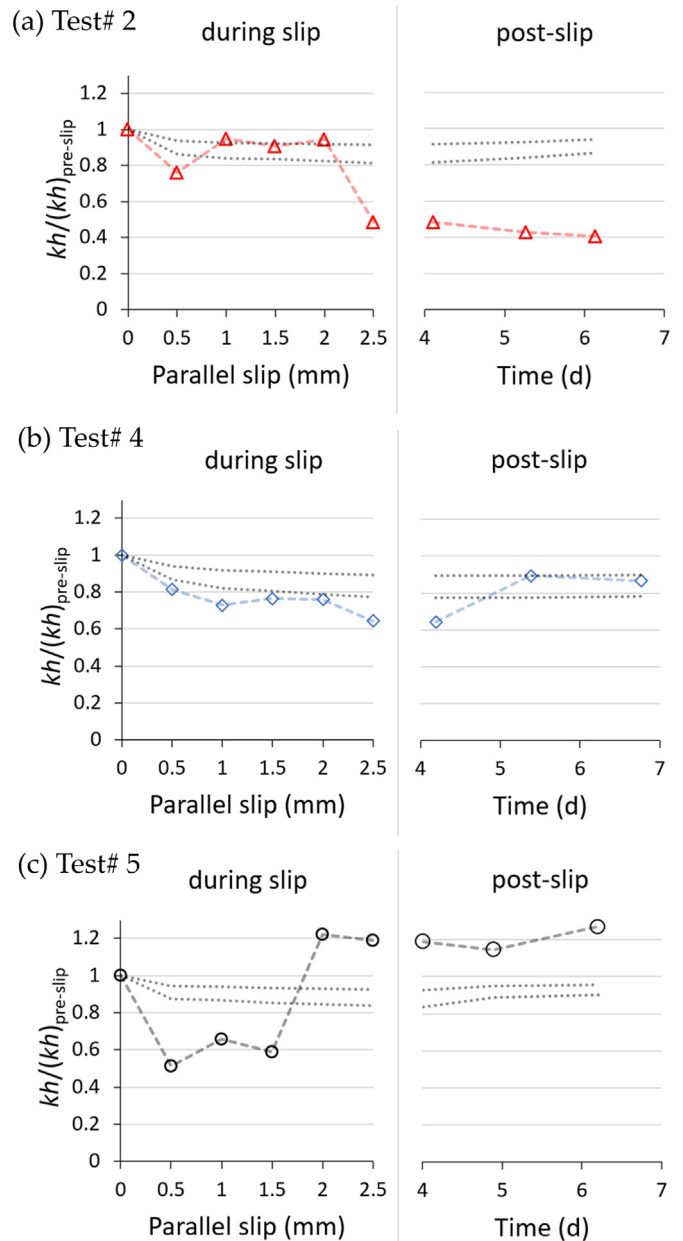


Fig. 11. Relative change to permeability during and post-slip for (a) Test #2, (b) Test #4, and (c) Test #5. Dashed lines represent projections for normal stress variation (using Equation (9)) as σ_n changes for C_m values of 0.035 MPa^{-1} (upper bound) and 0.08 MPa^{-1} (lower bound). Time in post-slip figures indicates time since CO_2 injection.

Samuelson and Spiers, 2012; Zoback and Kohli, 2019) with a trend of decreasing friction coefficient as clay content increases. It is hypothesized that clay minerals "lubricate" the system and reduce highly stressed grain contact points (Crawford et al., 2008). Nevertheless, our weak dependence on clay + kerogen content could be justified for the following reasons. First, we need to emphasize the different configurations of slipped cracks where gouges were tested in all before-mentioned tests (including Zoback and Kohli (2019)) under water or dry conditions. Using gouges reduces the problem of frictional behavior of shale to a question of shale mineralogy in the gouge, removing the potential role of rock fabric and rock mechanical properties. On the other hand, in our case of utilizing #100-grit saw-cut fractures, bare surfaces may

have a distribution of sliding contacts that is not as representative of the mineralogy as gouge.

Another factor is the utilization of binary and ternary mineral composition, mainly quartz with clay minerals, of gouges to the majority of before-mentioned studies. This approach does not incorporate the complexity of mineral composition, especially carbonate minerals, and mechanical interaction of intact asperities in saw-cut faults that exist in our study. Finally, mismatch of high clay content data to (Zoback and Kohli, 2019) might be explained by the maturity of our samples. Zoback and Kohli (2019) tested high kerogen content that has unique mechanical and reactive properties, and that might be the reason for such differences. The illustrated comparison in Fig. 10 highlights the different behavior between filled and unfilled cracks, that should be considered to predict the behavior of various crack types.

From a friction coefficient perspective, it is unlikely that saturating with CO₂ altered frictional strength parameters. As mentioned earlier, friction coefficient magnitudes fall in the upper range, that is a natural outcome of the conditions of carbonate-rich and relatively low clay-content samples with saw-cut fractures. Unfortunately, to our knowledge, there is no available data for Wolfcamp shale frictional strength parameters for comparison to our results. Other parameters, such as initial friction coefficient and strain hardening, did not show unique behavior because of sc-CO₂ saturation. Nevertheless, similar observations of no influence of sc-CO₂ saturation on friction coefficient has been reported. For instance, (Bakker et al., 2016) observed no significant influence of sc-CO₂ exposure for sandstone and carbonate rich gouges, and similarly for dry and wet gouges at a variety of clay-content by Samuelson and Spiers (2012). Moreover, Meng et al. (2021) observed a minor reduction in friction coefficient of 5%. While these findings align with ours, we suggest further investigation of other factors that are not considered in these studies. For example, samples with variation to reactive materials to sc-CO₂ should be tested, such materials are kerogen and clay minerals that demonstrate reactivity such as smectite and mixed layer clays. Other factors such as incubation period, rock porosity and water content should be investigated.

4.2. Permeability evolution

Transmissivity magnitudes in this study fall within reported values in the literature (Rutter and Mecklenburgh, 2018). Compared to their work, transmissivity values obtained using the steady-state approach (Tests #1, 2, and 5) fall in the range of hard rocks (sandstone and granite), while the only measurement with the modified pulse decay method (Tests #4) matches their Bowland shale samples. However, transmissivity measurements in our study do not correlate with either mineral composition or fault surface roughness, in the case of final transmissivity. Furthermore, there is no correlation between transmissivity and friction coefficient. In Test #1, where it simulates a quick pressure buildup within the fault triggering a slip, saturating with sc-CO₂ for a short period drastically reduced transmissivity. For controlled axial displacement tests that mimic a slow pressure buildup as consequence of sc-CO₂ invasion, net transmissivity change is also negative.

4.2.1. Saturation effect

Saturating with sc-CO₂ before slip (Test #2 and 5) and after slip (Test #1) resulted in a transmissivity drop (Figs. 5b and 6b). A very limited number of studies explored the fracture permeability evolution for dry samples under CO₂ exposure. Zhou et al. (2020) observed a permeability decrease as time increases during CO₂

exposure to Silurian Longmaxi shale for 24 h. They anticipate induced swelling to cause this reduction. On the other hand, Li et al. (2017) observed minimal change to fractures filled with a mono-layer proppant after 1 d of sc-CO₂ exposure, where they tested Green River shale samples.

Under constant stresses, fracture permeability decrease with sc-CO₂ saturation could be an outcome of the processes of mineral dissolution of fracture surfaces, salt precipitation, and adsorption into clay and organic matter (Abdoulghafour et al., 2016; Bhuiyan et al., 2020; He et al., 2022). For instance, Kamali-Asl et al. (2021) observed an alteration to calcite grain surfaces by dissolution after CO₂ saturation. Moreover, precipitation of halite and anhydrite formed on surfaces was noted due to the evaporation of residual water by sc-CO₂ (Lu et al., 2016). Nevertheless, mineral dissolution of fracture surfaces, and subsequent precipitation is expected to have a minimal impact in our test because of the almost complete absence of water on fracture surfaces. The samples were originally received dry, then vacuumed and heated to 45 °C for a minimum of two weeks prior to testing.

Adsorption induced swelling and the CO₂ corrosion induced weakening of matrix are the most likely mechanisms to damage fracture permeability over time. Several studies reported the significance of adsorption induced swelling. For instance, Hou et al. (2020) quantified embedment and swelling of Green River shale samples with a single fracture filled with a mono-layer proppant after CO₂ saturation. They tested originally dry samples at various pore pressures. Adsorption induced swelling contributed 9%–56% of aperture reduction. Furthermore, Kumar et al. (2015) reported larger permeability reduction for mono-layer proppant filled fractures compared to multi-layers. This highlights the significance of the swelling mechanism as the original aperture decreases. In fact, it is believed that CO₂ induced swelling of clay and kerogen has a major contribution to the sealing of small fractures (Zhang et al., 2018). The contribution of swelling is expected to correlate with clay and kerogen content. Nevertheless, no correlation between permeability reduction and clay + kerogen content is demonstrated in our data. This might be explained by the anisotropy of their distribution, where more influence might be observed when they are concentrated around the fracture vicinity. It is worth reminding the reader that we tested vertical samples (bedding planes are perpendicular to the sample axis), that results in large degree of mineralogical anisotropy on the face of the fracture tilted 30° from vertical.

On the other hand, the reactivity induced by CO₂ and water may deteriorate the strength of shale, even in the presence of only residual and clay-bound water. This was reported by Meng et al. (2021) when they observed a reduction in the amount of carbonate minerals of originally dried samples within short periods. They hypothesized that carbonate mineral dissolution weakens the connection between mineral grains, and subsequently reduces mechanical strength. The Young's modulus of samples dropped by 27% within 3 d.

We hypothesize that the combination of adsorption induced swelling and the mechanical weakening of dry shale samples by sc-CO₂ exposure enhances mating of fracture faces and reduces the aperture of thin cracks, resulting in permeability reduction. Further reduction is anticipated in the case of high water content because of reactivity. Hence, quantifying the contribution of water content is recommended for future work.

4.2.2. Slip effect

Without accounting for the influence of normal stress, results in Section 3.2 indicate that fault slip caused permeability reduction for

two samples, and enhancement for one (Fig. 6c). Because normal stress strongly affects permeability measurements, it is necessary to correct transmissivity measurements during and post slip. During slip, as a consequence of both constant axial displacement -while confining pressure is constant- and strain hardening, normal stress (σ_n) increases. To account for σ_n effects, projections of transmissivity measurements change as a result of solely normal stress should be calculated. In the literature, permeability shows an exponential decrease with increasing normal stress (Wu et al., 2017; Van Stappen et al., 2018; Rutter and Mecklenburgh, 2018; Zhou et al., 2020; Zhang and Talandier, 2023). Wu et al. (2017) proposed that stress-dependent permeability is well described by the following equation:

$$k(\sigma_{\text{eff}}) = k_0 e^{-C_m \sigma_{\text{eff}}} \quad (9)$$

where σ_{eff} is equivalent to the normal stress (σ_n) in our case, k_0 is the permeability at $\sigma_{\text{eff}} = 0$, C_m is the stress sensitivity coefficient. They calculated C_m for several saw-cut and natural fractures, before and after slip. For saw-cut samples, C_m ranged between 0.035 MPa^{-1} and 0.08 MPa^{-1} . We used the two values of C_m to project permeability change while excluding the slip effect for controlled axial displacement tests (Fig. 11). The dashed lines in each figure are the generated bounds stress-induced permeability change, where the upper line represents $C_m = 0.035$ and the lower bound is for a value of 0.08.

For all tests, the first 0.5 mm of slip results in a sharp permeability drop that is larger than the effect of increasing normal stress. This could be explained by the compaction and asperity collapse (Wang et al., 2020). Following the early permeability drop, transmissivity measurements demonstrated a stabilization or recovery for a couple of slip intervals. This recovery could be justified by a dilatation effect overcoming the initial drop, in addition to the effect of slip-hold-slip every 0.5 mm interval. It is reported in the literature that holding after inducing a slip then reactivating (slip-hold-slip) causes permeability increase by destroying asperity contacts, and permeability enhancement increases as the number of hold-slip steps increases (Im et al., 2018). At the final slip steps, two samples demonstrated further permeability reduction while one sample (Test #5) showed a huge permeability recovery to exceed the pre-slip transmissivity value. Finally, relaxation after slip (for 2–3 d) helped recover permeability for Test #4 and 5, while Test #2 demonstrated further transmissivity reduction.

Overall, relaxed slipped faults revealed permeability enhancement, reduction, and no change. These observations do not correlate with either frictional strength, surface topography, or mineralogy. In fact, it is difficult to separate the contribution of different mechanisms to the overall behavior because of the fine grain size and complex mineralogy of samples. However, we hypothesize the very smooth surfaces of tested faults to amplify the sensitivity to the winner in the competition between dilatation and the impact of debris. While dilatation increases permeability, wear products block flow paths. In fact, we believe that debris blockage is the main controller of the permeability of these smooth cracks during slip.

4.3. Implications for field applications

Our friction coefficient findings suggest that cracks within the caprock and stimulated unconventional reservoirs are expected to slip under typical pore pressure conditions. This critical finding ensures the integrity of seal formations to CO_2 storage formations when pore pressure is maintained below the Mohr Coulomb

criteria. In addition, the slippage behavior is different between cracks and gouge-filled cracks. Mineralogy dependence is pronounced in the latter case.

The novel approach in this study to quantify the combined effect of sc- CO_2 exposure and slippage on cracks transport reveals valuable insights. The net permeability reduction confirms that slipping cracks within shale sealing formations is not detrimental to its integrity. From a stimulation perspective, the observed negative net impact on permeability should still be compared to that of water for proper evaluation. It is worth mentioning that the contribution of crack extension towards transport should be investigated for a comprehensive analysis.

5. Conclusions

We investigated the frictional and transport behavior of dry fractures subjected to CO_2 injection under in situ stress conditions. We simulated fault slip during sc- CO_2 injection as a stimulation agent by abruptly and hydraulically inducing slip for one sample. Furthermore, we simulated the slow pressure buildup experienced by caprock formations by using constant slip rates in four tests.

Measured friction coefficients revealed large magnitudes indicative of hard rocks and as expected for carbonate-rich samples with relatively low clay content. Interestingly, the magnitude of friction coefficient shows no correlation to clay content for the moderate clay-content sample. This highlights the difference of frictional behavior compared to gouge filled tests where the impact of rock fabric and rock mechanical properties is captured. We find no clear impact of short-term sc- CO_2 saturation on frictional behavior in the absence of water.

Permeability evolution was quantified by calculating fault transmissivity that measures transport capacity for our specific fault configuration. We evaluated the influence of three processes: saturating with sc- CO_2 , fault slippage, and short-term relaxation after slip. Saturation significantly impairs fracture permeability even within a short time. This effect might be explained by adsorption induced swelling and matrix mechanical weakening that improve mating of fracture faces. Fault slippage with short time healing demonstrated variable permeability evolution. Our hypothesis is that smooth faults are extremely sensitive to the competition between permeability enhancement due to dilatation, and damage caused by debris blockage. Overall, the combined effect of saturation and slip upon transport within thin cracks is permeability reduction.

Our observations support the integrity of shale formation seals under sc- CO_2 conditions. As sc- CO_2 permeates into shale caprock and potentially activates displacement of thin cracks as a consequence of pressure buildup, the net impact of saturation and slip towards permeability is expected to be negative. On the other hand, our permeability results are not promising from a stimulation perspective for unproped sc- CO_2 injection. Factors not incorporated in our experiments might significantly overcome the local decrease of crack permeability such as an abrupt increase in pore pressure that unstably extends cracks, that solely, or with the intersection with other faults and cracks, enhances productivity of reservoir stimulated volume.

Declaration of competing interest

The authors declare that they have no known competing financial interests or personal relationships that could have appeared to influence the work reported in this paper.

List of symbols.

β_D	Downstream storativity
ΔP	Difference between upstream pressure and downstream pressure
η	Fluid viscosity
κ_f	Fluid compressibility
μ	Friction coefficient
σ_{eff}	Effective normal stress (Wu et al. (2017) notation)
σ_n	Effective normal stress
σ_1	Maximum stress (axial stress in our case)
σ_3	Minimum stress (radial stress in our case)
τ	Shear stress
θ	Fault angle from sample axis
a	Half the distance between wellbores across the fault
C_m	Stress sensitivity coefficient
f_1	Function that accounts for non-zero sample porosity
K	Hydraulic conductivity
k	Permeability
k_f	Fault permeability
kh	Fault transmissivity
kt	Fault transmissivity (Rutter and Mecklenburgh (2018) notation)
M	slope of the straight line in $\log_e(P(t)/P(0))$ vs. time plot
N	Number of line roughness calculations
P	Pressure
P_{dn}	Downstream pressure
P_p	Pore pressure
P_{up}	Upstream pressure
Q	Flow rate
r_0	Wellbore radius
R_p	Maximum peak height above mean line (Multi-line roughness)
R_v	Maximum valley depth below mean line (Multi-line roughness)
Re	Reynolds number
S_a	Arithmetic average of $z(x, y)$ (Surface roughness)
S_q	Quadratic average of $z(x, y)$ (Surface roughness)
t	Time
V_D	Downstream volume
w	Fault thickness for permeability calculations
$z(x, y)$	Height from mean line

Acknowledgments

This work was supported as part of the Center for Mechanistic Control of Unconventional Formations (CMC-UF), an Energy Frontier Research Center funded by the U.S. Department of Energy, Office of Science under DOE(BES) Award DE-SC0019165. We also thank King Fahd University (KFUPM) for granting a scholarship to the first author. Part of this work was performed at Stanford Nano Shared Facilities (SNSF) with support from NSF under award CMMI-1532224. SNSF is additionally supported by the NSF as part of the National Nanotechnology Coordinated Infrastructure under award ECCS-1542152.

References

Abdoulghafour, H., Gouze, P., Luquot, L., Leprovost, R., 2016. Characterization and modeling of the alteration of fractured class-g portland cement during flow of co₂-rich brine. *Int. J. Greenh. Gas Control* 48, 155–170.

Akono, A.-T., Druhan, J.L., Dávila, G., Tsotsis, T., Jessen, K., Fuchs, S., Crandall, D., Shi, Z., Dalton, L., Tkach, M.K., et al., 2019. A review of geochemical–mechanical impacts in geological carbon storage reservoirs. *Greenh. Gases: Sci. Technol.* 9 (3), 474–504.

Al Shafloot, T., 2022. Investigating the Performance of Supercritical Carbon Dioxide as a Stimulation Agent in Shale. PhD thesis. Stanford University.

Al Shafloot, T., Kim, T.W., Kovscek, A.R., 2021. Investigating fracture propagation characteristics in shale using sc-co₂ and water with the aid of x-ray computed tomography. *J. Nat. Gas Sci. Eng.* 92, 103736.

Aljamaan, H., Al Ismail, M., Kovscek, A.R., 2017. Experimental investigation and grand canonical Monte Carlo simulation of gas shale adsorption from the macro to the nano scale. *J. Nat. Gas Sci. Eng.* 48, 119–137.

Bakker, E., Hangx, S.J., Niemeijer, A.R., Spiers, C.J., 2016. Frictional behaviour and transport properties of simulated fault gouges derived from a natural co₂ reservoir. *Int. J. Greenh. Gas Control* 54, 70–83.

Bhuiyan, M.H., Agofack, N., Gawel, K.M., Cerasi, P.R., 2020. Micro-and macroscale consequences of interactions between co₂ and shale rocks. *Energies* 13 (5), 1167.

Bijay, K., Ghazanfari, E., Frash, L.P., 2023. Experimental study of fracture slip due to stress perturbation in fractured geo-resources. *Geomech. Energy Environ.* 33, 100423.

Byerlee, J., 1978. Friction of rocks. In: *Rock Friction and Earthquake Prediction*. Springer, pp. 615–626.

Carey, J.W., Lei, Z., Rougier, E., Mori, H., Viswanathan, H., 2015. Fracture-permeability behavior of shale. *J. Unconvent. Oil Gas Resour.* 11, 27–43.

Crawford, B., Faulkner, D., Rutter, E., 2008. Strength, porosity, and permeability development during hydrostatic and shear loading of synthetic quartz-clay fault gouge. *J. Geophys. Res. Solid Earth* 113 (B3), B004634.

Fang, Y., Elsworth, D., Wang, C., Jia, Y., 2018. Mineralogical controls on frictional strength, stability, and shear permeability evolution of fractures. *J. Geophys. Res. Solid Earth* 123 (5), 3549–3563.

Foroutan, M., Ghazanfari, E., Amirlatif, A., Moradian, O., 2022. Evolution of fracture permeability and aperture during co₂ storage in variably cemented sedimentary rocks. *Geomech. Energy Environ.* 32, 100289.

Freeze, R., Cherry, J., 1979. *Groundwater*. Prentice-hall.

Gandossi, L., et al., 2013. An overview of hydraulic fracturing and other formation stimulation technologies for shale gas production. *Eur. Commision Jt. Res. Cent. Tech. Rep.*, 26347.

Germanovich, L.N., Astakhov, D.K., 2004. Fracture closure in extension and mechanical interaction of parallel joints. *J. Geophys. Res. Solid Earth* 109 (B2), B002131.

Glatz, G., Lapene, A., Castanier, L.M., Kovscek, A.R., 2018. An experimental platform for triaxial high-pressure/high-temperature testing of rocks using computed tomography. *Rev. Sci. Instrum.* 89 (4), 045101.

Gundogar, A.S., Druhan, J.D., Ross, C.M., Jew, A.D., Bargar, J.R., Kovscek, A.R., 2022. Coreflood effluent and shale surface chemistries in predicting interaction between shale, brine, and reactive fluid. *SPE J.* 27 (4), 2283–2293.

Gundogar, A.S., Ross, C.M., Jew, A.D., Bargar, J.R., Kovscek, A.R., 2021. Multiphysics investigation of geochemical alterations in marcellus shale using reactive corefloods. *Energy Fuel* 35 (13), 10733–10745.

Gutierrez, M., Katsuki, D., Tutuncu, A., 2015. Determination of the continuous stress-dependent permeability, compressibility and poroelasticity of shale. *Mar. Petrol. Geol.* 68, 614–628.

He, D., Xu, R., Ji, T., Jiang, P., 2022. Experimental investigation of the mechanism of salt precipitation in the fracture during co₂ geological sequestration. *Int. J. Greenh. Gas Control* 118, 103693.

Hou, L., Elsworth, D., Geng, X., 2020. Swelling and embedment induced by sub-and super-critical-co₂ on the permeability of propped fractures in shale. *Int. J. Coal Geol.* 225, 103496.

Ikari, M.J., Saffer, D.M., Marone, C., 2009. Frictional and hydrologic properties of clay-rich fault gouge. *J. Geophys. Res. Solid Earth* 114 (B5), B006089.

Im, K., Elsworth, D., Fang, Y., 2018. The influence of pre-slip sealing on the permeability evolution of fractures and faults. *Geophys. Res. Lett.* 45 (1), 166–175.

Jew, A.D., Dustin, M.K., Harrison, A.L., Joe-Wong, C.M., Thomas, D.L., Maher, K., Brown Jr, G.E., Bargar, J.R., 2017. Impact of organics and carbonates on the oxidation and precipitation of iron during hydraulic fracturing of shale. *Energy Fuel* 31 (4), 3643–3658.

Jia, Y., Lu, Y., Elsworth, D., Fang, Y., Tang, J., 2018. Surface characteristics and permeability enhancement of shale fractures due to water and supercritical carbon dioxide fracturing. *J. Petrol. Sci. Eng.* 165, 284–297.

Kamali-Asl, A., Zoback, M.D., Kohli, A.H., 2021. Effects of supercritical co₂ on matrix permeability of unconventional formations. *Energies* 14 (4), 1101.

Kohli, A.H., Zoback, M.D., 2013. Frictional properties of shale reservoir rocks. *J. Geophys. Res. Solid Earth* 118 (9), 5109–5125.

Kolawole, O., Ispas, I., Kumar, M., Weber, J., Zhao, B., Zhanoni, G., 2021. How can biogeomechanical alterations in shales impact caprock integrity and co₂ storage? *Fuel* 291, 120149.

Kumar, H., Elsworth, D., Liu, J., Pone, D., Mathews, J.P., 2015. Permeability evolution of propped artificial fractures in coal on injection of co₂. *J. Petrol. Sci. Eng.* 133, 695–704.

Li, X., Feng, Z., Han, G., Elsworth, D., Marone, C., Saffer, D., Cheon, D.-S., 2017. Permeability evolution of propped artificial fractures in green river shale. *Rock Mech. Rock Eng.* 50 (6), 1473–1485.

Lu, J., Nicot, J.-P., Mickler, P.J., Ribeiro, L.H., Darviri, R., 2016. Alteration of bakken reservoir rock during co₂-based fracturing—an autoclave reaction experiment. *J. Unconvent. Oil Gas Resour.* 14, 72–85.

Meng, F., Wang, F., Wong, L.N.Y., Song, J., Li, M., Zhang, C., Zhang, L., 2023. Shear behavior and off-fault damage of saw-cut smooth and tension-induced rough joints in granite. *J. Rock Mech. Geotech. Eng.* 16(4), 1216–1230.

Meng, S., Jin, X., Tao, J., Wang, X., Zhang, C., 2021. Evolution characteristics of mechanical properties under supercritical carbon dioxide treatment in shale reservoirs. *ACS Omega* 6 (4), 2813–2823.

Middleton, R.S., Carey, J.W., Currier, R.P., Hyman, J.D., Kang, Q., Karra, S., Jiménez-Martínez, J., Porter, M.L., Viswanathan, H.S., 2015. Shale gas and non-aqueous fracturing fluids: opportunities and challenges for supercritical co₂. *Appl. Energy* 147, 500–509.

Moore, D.E., Lockner, D.A., 2004. Crystallographic controls on the frictional behavior of dry and water-saturated sheet structure minerals. *J. Geophys. Res. Solid Earth* 109 (B3), B002582.

Ozotta, O., Kolawole, O., Malki, M.L., Ore, T., Gentzis, T., Fowler, H., Liu, K., Ostadhassan, M., 2022. Nano-to macro-scale structural, mineralogical, and mechanical alterations in a shale reservoir induced by exposure to supercritical co₂. *Appl. Energy* 326, 120051.

- Polak, A., Elsworth, D., Liu, J., Grader, A.S., 2004. Spontaneous switching of permeability changes in a limestone fracture with net dissolution. *Water Resour. Res.* 40 (3), W03502.
- Power, W.L., Tullis, T.E., Weeks, J.D., 1988. Roughness and wear during brittle faulting. *J. Geophys. Res. Solid Earth* 93 (B12), 15268–15278.
- Rafatian, N., Capsan, J., 2015. Petrophysical characterization of the pore space in permian wolfcamp rocks. *Petrophys. SPWLA J. Format. Evaluat. Reservoir Descript.* 56 (1), 45–57.
- Rutter, E.H., Mecklenburgh, J., 2018. Influence of normal and shear stress on the hydraulic transmissivity of thin cracks in a tight quartz sandstone, a granite, and a shale. *J. Geophys. Res. Solid Earth* 123 (2), 1262–1285.
- Samuelson, J., Spiers, C.J., 2012. Fault friction and slip stability not affected by CO₂ storage: evidence from short-term laboratory experiments on north sea reservoir sandstones and caprocks. *Int. J. Greenh. Gas Control* 11, S78–S90.
- Sayers, C.M., Dasgupta, S., Koesoemadinata, A., Shoemaker, M., 2019. Rock physics of the wolfcamp formation, Delaware basin. *Geophysics* 84 (6), B353–B361.
- Scott, D.R., Lockner, D.A., Byerlee, J.D., Sammis, C.G., 1994. Triaxial testing of lopez fault gouge at 150 mpa mean effective stress. *Pure Appl. Geophys.* 142 (3), 749–775.
- Spokas, K., Fang, Y., Fitts, J., Peters, C., Elsworth, D., 2019. Collapse of reacted fracture surface decreases permeability and frictional strength. *J. Geophys. Res. Solid Earth* 124 (12), 12799–12811.
- Streit, J.E., Hillis, R.R., 2004. Estimating fault stability and sustainable fluid pressures for underground storage of CO₂ in porous rock. *Energy* 29 (9–10), 1445–1456.
- Taron, J., Elsworth, D., 2010. Coupled mechanical and chemical processes in engineered geothermal reservoirs with dynamic permeability. *Int. J. Rock Mech. Min. Sci.* 47 (8), 1339–1348.
- Tembe, S., Lockner, D.A., Wong, T.-F., 2010. Effect of clay content and mineralogy on frictional sliding behavior of simulated gouges: binary and ternary mixtures of quartz, illite, and montmorillonite. *J. Geophys. Res. Solid Earth* 115 (B3), B006383.
- Van Stappen, J.F., Meftah, R., Boone, M.A., Bultreys, T., De Kock, T., Blykers, B.K., Senger, K., Olaussen, S., Cnudde, V., 2018. In situ triaxial testing to determine fracture permeability and aperture distribution for CO₂ sequestration in svalbard, Norway. *Environ. Sci. Technol.* 52 (8), 4546–4554.
- Wang, C., Elsworth, D., Fang, Y., Zhang, F., 2020. Influence of fracture roughness on shear strength, slip stability and permeability: a mechanistic analysis by three-dimensional digital rock modeling. *J. Rock Mech. Geotech. Eng.* 12 (4), 720–731.
- Witherspoon, P.A., Wang, J.S., Iwai, K., Gale, J.E., 1980. Validity of cubic law for fluid flow in a deformable rock fracture. *Water Resour. Res.* 16 (6), 1016–1024.
- Wu, W., Reece, J.S., Gensterblum, Y., Zoback, M.D., 2017. Permeability evolution of slowly slipping faults in shale reservoirs. *Geophys. Res. Lett.* 44 (22), 11–368.
- Yeo, I., De Freitas, M., Zimmerman, R., 1998. Effect of shear displacement on the aperture and permeability of a rock fracture. *Int. J. Rock Mech. Min. Sci.* 35 (8), 1051–1070.
- Zakhour, N., Shoemaker, M., Lee, D., 2015. Integrated workflow using 3d seismic and geomechanical properties with microseismic and stimulation data to optimize completion methodologies: wolfcamp shale-oil play case study in the midland basin. In: *SPE Eastern Regional Meeting*. OnePetro.
- Zhang, B., Yang, F., Hu, D., Zhou, H., 2023a. Laboratory study on injection-induced fault activation and slip behavior on fractures with specified roughness in sandstone. *Rock Mech. Rock Eng.* 1–20.
- Zhang, C., Xu, J., Jin, S., Cui, G., Guo, Y., Li, L., 2023b. Sliding modes of fault activation under constant normal stiffness conditions. *J. Rock Mech. Geotech. Eng.* 15 (5), 1213–1225.
- Zhang, C.-L., Talandier, J., 2023. Self-sealing of fractures in indurated claystones measured by water and gas flow. *J. Rock Mech. Geotech. Eng.* 15 (1), 227–238.
- Zhang, G., Zhou, D., Wang, P., Zhang, K., Tang, M., 2020. Influence of supercritical CO₂-water on the micromechanical properties of sandstone. *Int. J. Greenh. Gas Control* 97, 103040.
- Zhang, M., de Jong, S., Spiers, C.J., Busch, A., Wentinck, H.M., 2018. Swelling stress development in confined smectite clays through exposure to CO₂. *Int. J. Greenh. Gas Control* 74, 49–61.
- Zhou, J., Tian, S., Zhou, L., Xian, X., Yang, K., Jiang, Y., Zhang, C., Guo, Y., 2020. Experimental investigation on the influence of sub-and super-critical CO₂ saturation time on the permeability of fractured shale. *Energy* 191, 116574.
- Zimmerman, R.W., Bodvarsson, G.S., 1996. Hydraulic conductivity of rock fractures. *Transport Porous Media* 23 (1), 1–30.
- Zoback, M.D., Kohli, A.H., 2019. *Unconventional Reservoir Geomechanics*. Cambridge University Press.



Dr. Talal Al Shafloot is an Assistant Professor in the petroleum engineering department at King Fahd University of Petroleum and Minerals. Talal obtained his Bachelor's degree in petroleum Engineering from KFUPM, Master's degree in petroleum engineering from Texas A&M University, and his PhD in petroleum engineering from Stanford University. During his PhD, he conducted an experimental campaign to investigate the geomechanical and transport aspects of shale when interacting with supercritical carbon dioxide (sc-CO₂) under in situ conditions. He specifically examined the behavior of tensile fractures, shear fractures, and visco-elastic/plastic behavior.

Talal's current research focuses on the geomechanical, transport, and storage characterization of unconventional formations when pressurized or saturated with various fluids of interest. One goal is examining the geomechanical and transport aspects of underground formations to ensure the integrity of seal formations. Understanding such aspect is crucial to predict the short and long-term impact of fluids injected into energy storage and CO₂ sequestration formations. Another goal is finding economically viable solutions for producing energy from unconventional resources by evaluating different fracture propagation mechanisms under the pressurization of potential stimulation candidates.